Speed of sound in magnetized nuclear matter

Rajkumar Mondal [1,3,*], Nilanjan Chaudhuri [1,3,†], Pradip Roy [2,3,‡] and Sourav Sarkar [1,3,§]

[1]*Variable Energy Cyclotron Centre, 1/AF Bidhannagar, Kolkata 700064, India*
[2]*Saha Institute of Nuclear Physics, 1/AF Bidhannagar, Kolkata 700064, India*
[3]*Homi Bhabha National Institute, Training School Complex, Anushaktinagar, Mumbai 400085, India*

Employing the nonlinear Walecka model we investigate the characteristics of nuclear matter under the influence of a background magnetic field at a finite temperature and baryon chemical potential. In the presence of the magnetic field the spinodal lines and the critical endpoint (CEP) undergo changes in the T-μ_B plane. The squared speed of sound exhibits anisotropic behavior, dividing into parallel and perpendicular components. Additionally, the presence of a magnetic field induces anisotropy in the isothermal compressibility. It is found that the parallel component is smaller than the perpendicular one for all values of temperature, chemical potential, and magnetic field, indicating that the equation of state is stiffer along the magnetic-field direction.

I. INTRODUCTION

The speed of sound, represented as C_x, is an important quantity intrinsic to all thermodynamic systems. In the context of fluid dynamics, it denotes the speed at which a longitudinal compression wave propagates through the medium. Mathematically, it is calculated as the square root of the ratio between a change in pressure p and a corresponding shift in energy density ϵ while holding x as a constant parameter employed in the calculation. Hence, it establishes a direct correlation with the thermodynamic properties of the system, including its equation of state (EoS).

In the domain of dense nuclear matter the speed of sound holds particular significance for neutron-star research. The variation of C_x with density has a substantial impact on the mass-radius relationship, cooling rate, the maximum possible mass of neutron star [1] and tidal deformability. Analysis of current neutron-star data indicates a substantial increase in C_x^2 at densities n_B beyond the nuclear saturation density n_0 [2–5]. Moreover, as indicated in Ref. [6], the speed of sound has crucial impact on the frequencies of gravitational waves generated by the *g*-mode oscillation of a neutron star.

Currently, the sole experimental method available for studying strongly interacting hot and/or dense matter in the laboratory is through relativistic heavy-ion collisions in which a new state of transient matter called quark-gluon plasma (QGP) is expected to be formed as a result of phase transition or crossover from hadronic matter at high temperature and/or density [7]. The first-principle lattice QCD (LQCD) calculations indicates that the transition from hadronic matter to QGP

is a smooth crossover at high temperature and low baryon chemical potential [8–11]. A first-order phase transition is predicted by few models at large chemical potential with a critical endpoint connecting with a crossover transition [12–14]. The investigation of nuclear matter at high baryon number densities n_B, as conducted by programs like the Beam Energy Scan at the Relativistic Heavy Ion Collider (RHIC) plays a particularly vital role in the search for the QCD critical point. During the space-time evolution of the QGP the speed of sound plays a crucial role emerges in characterizing the EoS which is an essential input to the hydrodynamic equations. The sensitivity of the speed of sound on temperature, density, chemical potential, etc. provides crucial insights: it exhibits a local minimum at a crossover transition, while it reaches zero at the critical point and along the corresponding spinodal lines. At a vanishing baryon chemical potential ($\mu_B = 0$), LQCD demonstrates a minimum in the speed of sound C_s at temperature $T_0 = 156.5 \pm 1.5$ MeV, signifying crossover transition between hadron gas and QGP [15]. The speed of sound in QCD matter has been computed using various methods including LQCD [8,10,11,16], the (Polyakov-)Nambu–Jona-Lasinio [(P)NJL] model [17–19], the quark-meson coupling model [20,21], the hadron resonance gas (HRG) model [22,23], the field correlator method (FCM) [24,25] and the quasiparticle model [26].

It is conjectured that in noncentral heavy ion collisions (HICs), a very strong magnetic field is generated due to the rapid movement of the electrically charged spectators during the initial phase of the collision. The estimated strength of this magnetic field is around 10^{15}–10^{18} Gauss [27–29] and it experiences a rapid decay within a few fm/c. However, owing to the finite conductivity (approximately a few MeV) of the produced medium, the decay of the magnetic field is significantly delayed, allowing a nonzero magnetic field to persist even during the subsequent hadronic phase, following the phase transition or crossover from the QGP [30–32]. All these estimations are done by including the effect of finite electrical

---

*rajkumarmondal.phy@gmail.com
†nilanjan.vecc@gmail.com; n.chaudhri@vecc.gov.in
‡pradipk.roy@saha.ac.in
§sourav@vecc.gov.in

054911-1

conductivity of the medium by using Ohm's law. However the validity of conventional Ohm's law in the context of a rapidly evolving quark-gluon plasma produced in HICs is a topic of an ongoing discussion [33,34]. It is argued that the rapidly expanding medium presents an incomplete electromagnetic response due to the fact that the relaxation time for the induced electric current towards Ohm's law is much larger than the lifetime of the external magnetic field created in noncentral HICs. Additionally the study of strongly interacting matter in the presence of background magnetic field is also relevant for astrophysical scenarios as such type of matter can also be found in the interior of magnetars [35,36].

The presence of magnetic field could lead to significant modifications in the properties of the hadronic matter, leading to extensive research in this area, a few notable examples of which we mention here. The impact of magnetic fields on transport properties within the hadronic medium has been studied in Refs. [32,37–41]. Additionally, estimates of shear and bulk viscosity from magnetically modified hadronic matter have been explored in various approaches in Refs. [37–40]. Furthermore, the effects of magnetic fields on the electrical conductivity of a strongly interacting hadron gas have been investigated in Refs. [32,41]. The present authors have also studied the dilepton production rate from magnetized hadronic medium in Refs. [42,43]. Reference [44] describes the effect of a constant background magnetic field on nucleon mass in a strongly interacting medium in the weak-field approximation within the Walecka model. Recently, in Ref. [45], the authors studied the speed of sound and liquid-gas phase transition in nuclear matter at finite temperature and density (chemical potential) using the nonlinear Walecka model. In this work, we study the nature of speed of sound and liquid-gas phase transition in nuclear matter in presence of background magnetic field in the framework of the nonlinear Walecka model. The range of temperature and baryon chemical potential investigated in this article are more suitable for the physical scenario of compact astrophysical objects such as a neutron star or magnetar. In addition we also investigate the isothermal compressibility in the presence of magnetic field.

The article is structured as follows: Section II provides a concise overview of the general formalism of the nonlinear Walecka model, while Sec. III presents expressions for the speed of sound in various thermodynamical situations. In Sec. IV, we investigate the results, followed by a summary and conclusion in Sec. V. Additional details can be found in the Appendix.

II. WALECKA MODEL

The Lagrangian density of the Walecka model, describing the nucleons-meson system, is given by

$$\mathcal{L} = \mathcal{L}_{\text{em}} + \mathcal{L}_{\mathcal{N}} + \mathcal{L}_{\text{mes}} + \mathcal{L}_{\mathcal{I}}. \tag{1}$$

Here, $\mathcal{L}_{\text{em}} = -\frac{1}{2} F_{\mu\nu} F^{\mu\nu}$ represents the free field part where $F_{\mu\nu}$ is the field tensor corresponding to the external magnetic field, $\mathcal{L}_{\mathcal{N}}$ describes nucleons in a magnetic field, $\mathcal{L}_{\text{mes}}$ denotes the free mesons and their self-interactions, and $\mathcal{L}_{\mathcal{I}}$ contains the interactions between nucleons mediated by the σ and ω

mesons:

$$\mathcal{L}_{\mathcal{N}} = \bar{\psi}(i\gamma^{\mu} D_{\mu} - m_N + \gamma^0 \mu_B)\psi, \tag{2}$$

$$\mathcal{L}_{\mathcal{I}} = g_{\sigma} \bar{\psi} \sigma \psi - g_{\omega} \bar{\psi} \gamma^{\mu} \omega_{\mu} \psi, \tag{3}$$

$$\mathcal{L}_{\text{mes}} = \frac{1}{2} \big(\partial_{\mu}\sigma \partial^{\mu}\sigma - m_{\sigma}^2 \sigma^2\big) - \frac{b}{3} m_N (g_{\sigma}\sigma)^3$$
$$- \frac{c}{4}(g_{\sigma}\sigma)^4 - \frac{1}{4}\omega_{\mu\nu}\omega^{\mu\nu} + \frac{1}{2}m_{\omega}^2\omega_{\mu}\omega^{\mu}, \tag{4}$$

where $\omega_{\mu\nu} = \partial_{\mu}\omega_{\nu} - \partial_{\nu}\omega_{\mu}$, ψ represents the nucleon isospin doublet, the covariant derivative $D_{\mu} = \partial_{\mu} + ieA_{\mu}$ with $A_{\mu} = (0, yB, 0, 0)$ representing a homogeneous background magnetic field in the z direction, and e is the electric charge of the proton.

We apply the mean-field approximation to calculate the free energy, i.e., we neglect the fluctuations around the background mesonic fields assumed to be uniform in space-time. Therefore, the dynamical mass and the effective chemical potential of nucleon are

$$M = m_N - g_{\sigma}\bar{\sigma}, \quad \mu^{\star} = \mu_B - g_{\omega}\bar{\omega}_0, \tag{5}$$

where $\bar{\sigma} = \langle \bar{\psi}\psi \rangle$ and $\bar{\omega}_0 = \langle \bar{\psi}\gamma^0\psi \rangle$.

The model parameters g_{σ}, g_{ω}, b, c are fitted in mean-field approximation to reproduce the properties of nuclear matter at saturation in absence of magnetic field such as the saturation density $n_0 = 0.153$ fm^{-3}, compression modulus $K = 240$ MeV, binding energy $E_{\text{bind}} = -16.3$ MeV, and the effective nucleon mass $M = 0.8 m_N$. This leads to the chemical potential $\mu_0 = 922.7$ MeV at saturation. The parameters are listed in Table I. [46]

In this model the free energy has the form

$$\Omega = \frac{B^2}{2} + U + \Omega_N. \tag{6}$$

$B^2/2$ stems from the magnetic field pointing in the z direction, i.e., $\boldsymbol{B}(0, 0, B)$, U is the tree-level potential given by

$$U = \frac{1}{2}m_{\sigma}^2\bar{\sigma}^2 + \frac{b}{3}m_N(g_{\sigma}\bar{\sigma})^3 + \frac{c}{4}(g_{\sigma}\bar{\sigma})^4 - \frac{1}{2}m_{\omega}^2\bar{\omega}_0^2, \tag{7}$$

and Ω_N is the nucleonic contribution to the free energy. It depends on the dynamical nucleon mass $M(B, \mu, T)$ which is determined by minimizing the free energy. We can decompose $\Omega_N(M, B, \mu, T)$ as

$$\Omega_N = \Omega_{\text{sea}} + \Omega_{\text{TM}}, \tag{8}$$

where Ω_{sea} contains pure vacuum as well as the magnetic-field-dependent vacuum contributions and Ω_{TM} is the thermomagnetic (TM) contribution to the free energy. We can write

TABLE I. Parameters in Walecka model.

m_σ(MeV)	m_ω(MeV)	m_N(MeV)	g_σ	g_ω	b	c
550	782	939	8.1617	8.5062	1.0784×10^{-2}	-6.2205×10^{-3}

the expressions as

$$\Omega_{\text{sea}} = -2 \int \frac{d^3k}{(2\pi)^3} E - \frac{eB}{2\pi} \sum_{n=0}^{\infty} \alpha_n \int \frac{dk_z}{2\pi} E_n \quad (9)$$

$$= \Omega_{\text{vac}} + \Omega_{\text{vac}}^B, \quad (10)$$

where $\alpha_n = 2 - \delta_{n0}$ arises due to the spin degeneracy of each Landau level (n), $E = (M^2 + k^2)^{1/2}$, $E_n = (M^2 + k_z^2 + 2neB)^{1/2}$ for the spin-1/2 fermion with electric charge e. We can drop the pure vacuum contribution Ω_{vac} by a redefinition of the free energy because the model employed is renormalizable [47]. Even if the contribution from Ω_{vac}

is included, Ref. [46] explicitly demonstrates by choosing a suitable renormalization scheme that it has a very small effect on the final results. Thus, we proceed with eB-dependent vacuum contributions Ω_{vac}^B which is given by (see Appendix A for details)

$$\Omega_{\text{vac}}^B = -\frac{(eB)^2}{2\pi^2} \left\{ \zeta'(-1, x) + \frac{1}{4}x^2 + \frac{1}{2}x(1-x) \ln x \right\}, \quad (11)$$

where $x = M^2/2eB$, $\zeta'(-1, x) = d\zeta(z, x)/dz|_{z=-1}$, and $\zeta(z, x)$ is Hurwitz zeta function. Furthermore, Ω_{TM} can be expressed as

$$\Omega_{\text{TM}} = 2\beta^{-1} \int \frac{d^3k}{(2\pi)^3} \{\ln(1 - f^+) + \ln(1 - f^-)\} + \beta^{-1} \frac{eB}{2\pi} \sum_{n=0}^{\infty} \alpha_n \int \frac{dp_z}{2\pi} \{\ln(1 - f_n^+) + \ln(1 - f_n^-)\}. \quad (12)$$

Here $f^\pm = f(E \mp \mu^\star)$, $f_n^\pm = f(E_n \mp \mu^\star)$, $\beta = 1/T$, $f(x) = 1/(e^{x/T} + 1)$ is the Fermi distribution function, and $+ (-)$ corresponds to the fermion (antifermion) distribution function. Now, minimizing the free energy, i.e., putting

$$\frac{\partial \Omega}{\partial \bar{\sigma}} = \frac{\partial \Omega}{\partial \bar{\omega}_0} = 0, \quad (13)$$

we get the equations

$$n_s = -\frac{M - m_N}{(g_\sigma/m_\sigma)^2} + bm_N(m_N - M)^2 + c(m_N - M)^3 + \frac{eB}{2\pi^2}M\left\{ x(1 - \ln x) + \frac{1}{2}\ln\frac{x}{2\pi} + \ln\Gamma(x) \right\}, \quad (14)$$

$$n_B = \frac{\mu_B - \mu^\star}{(g_\omega/m_\omega)^2}, \quad (15)$$

where we have defined the scalar and baryon densities as

$$n_s = 2 \int \frac{d^3k}{(2\pi)^3} \frac{M}{E}(f^+ + f^-) + \frac{eB}{2\pi} \sum_{n=0}^{\infty} \alpha_n \int \frac{dk_z}{(2\pi)} \frac{M}{E_n}(f_n^+ + f_n^-), \quad (16)$$

$$n_B = 2 \int \frac{d^3k}{(2\pi)^3}(f^+ - f^-) + \frac{eB}{2\pi} \sum_{n=0}^{\infty} \alpha_n \int \frac{dk_z}{(2\pi)}(f_n^+ - f_n^-). \quad (17)$$

Both n_s and n_B contain contributions from neutrons and protons, while the term within second brackets in Eq. (14) is the renormalized term coming from the derivative $\partial\Omega_{\text{sea}}/\partial M$ which contributes only for protons. Furthermore, the expressions for entropy density and magnetization are as follows:

$$s = -\frac{\partial\Omega}{\partial T} = -2 \int \frac{d^3k}{(2\pi)^3} \left\{ \ln(1 - f^+) + \ln(1 - f^-) - \frac{E}{T}(f^+ + f^-) + \frac{\mu^\star}{T}(f^+ - f^-) \right\}$$

$$- \frac{eB}{2\pi} \sum_{n=0}^{\infty} \alpha_n \int \frac{dk_z}{2\pi} \left\{ \ln(1 - f_n^+) + \ln(1 - f_n^-) - \frac{E_n}{T}(f_n^+ + f_n^-) + \frac{\mu^\star}{T}(f_n^+ - f_n^-) \right\}, \quad (18)$$

$$\mathcal{M} = -\frac{\partial\Omega}{\partial B} = -B - e\left[\frac{eB}{2\pi^2}x\left\{ x(1 - \ln x) + \ln\Gamma(x) + \frac{1}{2}\ln\frac{x}{2\pi} \right\} \right.$$

$$\left. - \frac{T}{2\pi} \sum_{n=0}^{\infty} \alpha_n \int \frac{dp_z}{2\pi} \{\ln(1 - f_n^+) + \ln(1 - f_n^-)\} - \frac{eB}{2\pi} \sum_{n=0}^{\infty} \alpha_n \int \frac{dp_z}{2\pi} \frac{n}{E_n}\{f_n^+ + f_n^-\} \right]. \quad (19)$$

III. SPEED OF SOUND

The general definition of the speed of sound requires the specification of a constant quantity x such as entropy density s, s/n_B, T, μ_B, etc. during the propagation of the compression wave through a medium. The squared speed of sound (C_x^2) is defined as

$$C_x^2 = \left(\frac{\partial p}{\partial \epsilon}\right)_x. \tag{20}$$

Here, p represents pressure and ϵ denotes energy density.

In relativistic HICs, the created ideal fluid evolves with constant s/n_B. This conclusion can be derived in hydrodynamics due to the conservation of energy and baryon number. Therefore, it is important to compute the squared speed of sound C_{s/n_B}^2 along the isentropic curve.

The other definitions of speed of sound found in literature at constant baryon number density or entropy are usually used to describe the intermediate stages of hydrodynamic evolution. Furthermore, it is also interesting to compute the squared speed of sound with constant temperature T and chemical potential μ_B. In this paper, we investigate the speed of sound in nuclear matter subjected to a background magnetic field in the T-μ_B plane. The expressions for energy density and the longitudinal and transverse components of the pressure are as follows [48,49]:

$$\epsilon = \Omega + Ts + \mu_B n_B, \tag{21}$$

$$p^\parallel = -\Omega, \quad p^\perp = p^\parallel - B\mathcal{M}. \tag{22}$$

Correspondingly, the speed of sound becomes anisotropic due to the presence of magnetic field. We specify the speed of sound using different thermodynamic relations expressed in terms of temperature T and baryon chemical potential μ_B as

$$C_x^2(T, \mu_B) = C_x^{2(\parallel)}(T, \mu_B) = \left(\frac{\partial p_\parallel}{\partial \epsilon}\right)_x$$

$$= \frac{\left(\frac{\partial p^\parallel}{\partial T}\right)_{\mu_B}\left(\frac{\partial x}{\partial \mu_B}\right)_T - \left(\frac{\partial p^\parallel}{\partial \mu_B}\right)_T\left(\frac{\partial x}{\partial T}\right)_{\mu_B}}{\left(\frac{\partial \epsilon}{\partial T}\right)_{\mu_B}\left(\frac{\partial x}{\partial \mu_B}\right)_T - \left(\frac{\partial \epsilon}{\partial \mu_B}\right)_T\left(\frac{\partial x}{\partial T}\right)_{\mu_B}}, \tag{23}$$

$$C_x^{2(\perp)}(T, \mu_B) = \left(\frac{\partial p_\perp}{\partial \epsilon}\right)_x = C_x^{2(\parallel)} - B\left(\frac{\partial \mathcal{M}}{\partial \epsilon}\right)_x$$

$$= C_x^{2(\parallel)} - B\frac{\left(\frac{\partial \mathcal{M}}{\partial T}\right)_{\mu_B}\left(\frac{\partial x}{\partial \mu_B}\right)_T - \left(\frac{\partial \mathcal{M}}{\partial \mu_B}\right)_T\left(\frac{\partial x}{\partial T}\right)_{\mu_B}}{\left(\frac{\partial \epsilon}{\partial T}\right)_{\mu_B}\left(\frac{\partial x}{\partial \mu_B}\right)_T - \left(\frac{\partial \epsilon}{\partial \mu_B}\right)_T\left(\frac{\partial x}{\partial T}\right)_{\mu_B}}, \tag{24}$$

where $C_x = C_x^{(\parallel)}$ and $C_x^{(\perp)}$ are the sound velocities along and perpendicular to the magnetic-field direction, respectively. Using the thermodynamic relation in Appendix B, we can further write down the sound velocity along the magnetic field as

$$C_{s/n_B}^{2(\parallel)} = \frac{n_B s\left(\frac{\partial s}{\partial \mu_B}\right)_T - s^2\left(\frac{\partial n_B}{\partial \mu_B}\right)_T - n_B^2\left(\frac{\partial s}{\partial T}\right)_{\mu_B} + s n_B\left(\frac{\partial n_B}{\partial T}\right)_{\mu_B}}{(sT + \mu_B n_B)\{\left(\frac{\partial s}{\partial \mu_B}\right)_T\left(\frac{\partial n_B}{\partial T}\right)_{\mu_B} - \left(\frac{\partial s}{\partial T}\right)_{\mu_B}\left(\frac{\partial n_B}{\partial \mu_B}\right)_T\}}, \tag{25}$$

$$C_{n_B}^{2(\parallel)} = \frac{s\left(\frac{\partial n_B}{\partial \mu_B}\right)_T - n_B\left(\frac{\partial n_B}{\partial T}\right)_{\mu_B}}{T\{\left(\frac{\partial s}{\partial T}\right)_{\mu_B}\left(\frac{\partial n_B}{\partial \mu_B}\right)_T - \left(\frac{\partial s}{\partial \mu_B}\right)_T\left(\frac{\partial n_B}{\partial T}\right)_{\mu_B}\}}, \tag{26}$$

$$C_s^{2(\parallel)} = \frac{s\left(\frac{\partial s}{\partial \mu_B}\right)_T - n_B\left(\frac{\partial s}{\partial T}\right)_{\mu_B}}{\mu_B\{\left(\frac{\partial s}{\partial \mu_B}\right)_T\left(\frac{\partial n_B}{\partial T}\right)_{\mu_B} - \left(\frac{\partial s}{\partial T}\right)_{\mu_B}\left(\frac{\partial n_B}{\partial \mu_B}\right)_T\}}, \tag{27}$$

$$C_T^{2(\parallel)} = \frac{n_B}{T\left(\frac{\partial s}{\partial \mu_B}\right)_T + \mu_B\left(\frac{\partial n_B}{\partial \mu_B}\right)_T}, \tag{28}$$

$$C_{\mu_B}^{2(\parallel)} = \frac{s}{T\left(\frac{\partial s}{\partial T}\right)_{\mu_B} + \mu_B\left(\frac{\partial n_B}{\partial T}\right)_{\mu_B}}, \tag{29}$$

and sound velocity perpendicular to the magnetic field as

$$C_{s/n_B}^{2(\perp)} = C_{s/n_B}^{2(\parallel)} - B\frac{n_B\{\left(\frac{\partial \mathcal{M}}{\partial T}\right)_{\mu_B}\left(\frac{\partial s}{\partial \mu_B}\right)_T - \left(\frac{\partial \mathcal{M}}{\partial \mu_B}\right)_T\left(\frac{\partial s}{\partial T}\right)_{\mu_B}\} - s\{\left(\frac{\partial \mathcal{M}}{\partial T}\right)_{\mu_B}\left(\frac{\partial n_B}{\partial \mu_B}\right)_T - \left(\frac{\partial \mathcal{M}}{\partial \mu_B}\right)_T\left(\frac{\partial n_B}{\partial T}\right)_{\mu_B}\}}{(sT + \mu_B n_B)\{\left(\frac{\partial s}{\partial \mu_B}\right)_T\left(\frac{\partial n_B}{\partial T}\right)_{\mu_B} - \left(\frac{\partial s}{\partial T}\right)_{\mu_B}\left(\frac{\partial n_B}{\partial \mu_B}\right)_T\}}, \tag{30}$$

$$C_{n_B}^{2(\perp)} = C_{n_B}^{2(\parallel)} - B\frac{\left(\frac{\partial \mathcal{M}}{\partial T}\right)_{\mu_B}\left(\frac{\partial n_B}{\partial \mu_B}\right)_T - \left(\frac{\partial \mathcal{M}}{\partial \mu_B}\right)_T\left(\frac{\partial n_B}{\partial T}\right)_{\mu_B}}{T\{\left(\frac{\partial s}{\partial T}\right)_{\mu_B}\left(\frac{\partial n_B}{\partial \mu_B}\right)_T - \left(\frac{\partial s}{\partial \mu_B}\right)_T\left(\frac{\partial n_B}{\partial T}\right)_{\mu_B}\}}, \tag{31}$$

$$C_s^{2(\perp)} = C_s^{2(\parallel)} - B\frac{\left(\frac{\partial \mathcal{M}}{\partial T}\right)_{\mu_B}\left(\frac{\partial s}{\partial \mu_B}\right)_T - \left(\frac{\partial \mathcal{M}}{\partial \mu_B}\right)_T\left(\frac{\partial s}{\partial T}\right)_{\mu_B}}{\mu_B\{\left(\frac{\partial s}{\partial \mu_B}\right)_T\left(\frac{\partial n_B}{\partial T}\right)_{\mu_B} - \left(\frac{\partial s}{\partial T}\right)_{\mu_B}\left(\frac{\partial n_B}{\partial \mu_B}\right)_T\}}, \tag{32}$$

$$C_T^{2(\perp)} = C_T^{2(\parallel)} - B\frac{\left(\frac{\partial \mathcal{M}}{\partial \mu_B}\right)_T}{T\left(\frac{\partial s}{\partial \mu_B}\right)_T + \mu_B\left(\frac{\partial n_B}{\partial \mu_B}\right)_T}, \tag{33}$$

$$C_{\mu_B}^{2(\perp)} = C_{\mu_B}^{2(\parallel)} - B\frac{\left(\frac{\partial \mathcal{M}}{\partial T}\right)_{\mu_B}}{T\left(\frac{\partial s}{\partial T}\right)_{\mu_B} + \mu_B\left(\frac{\partial n_B}{\partial T}\right)_{\mu_B}}, \tag{34}$$
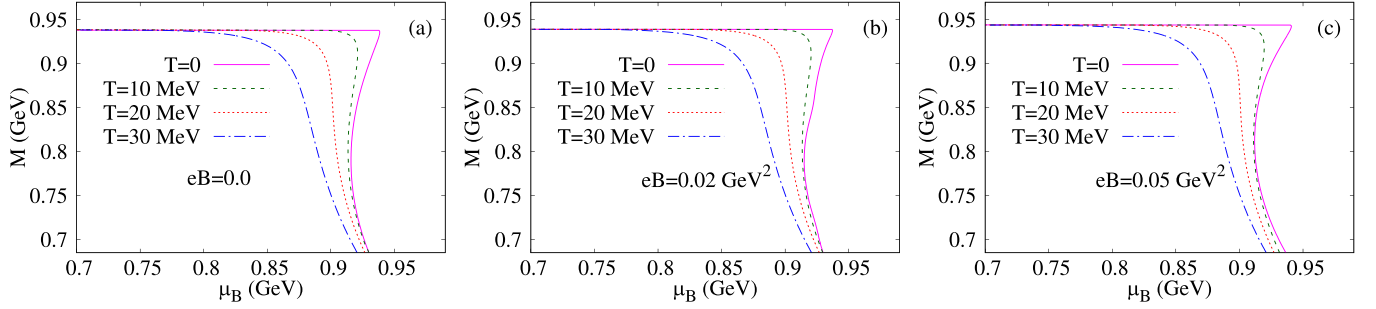
FIG. 1. The effective nucleon mass (M) as a function of baryon chemical potential (μ_B) for different values of temperatures $T = 0$, 10, 20, 30 MeV at (a) $eB = 0$, (b) $eB = 0.02$ GeV^2, (c) $eB = 0.05$ GeV^2.

where the analytical expressions for the derivatives $(\partial \mathcal{M}/\partial T)_{\mu_B}$, $(\partial \mathcal{M}/\partial \mu_B)_T$, $(\partial s/\partial \mu_B)_T$, $(\partial s/\partial T)_{\mu_B}$, $(\partial n_B/\partial \mu_B)_T$, $(\partial n_B/\partial T)_{\mu_B}$ are provided in Appendix C.

In the case of zero magnetic field, the isothermal compressibility of the medium is defined by the relation

$$K_T = \frac{1}{n_B} \frac{\frac{\partial n_B}{\partial \mu_B}}{\frac{\partial p}{\partial \mu_B}} = \frac{1}{n_B^2} \left(\frac{\partial n_B}{\partial \mu_B} \right)_T. \tag{35}$$

Due to the anisotropy in pressure K_T splits into parallel and perpendicular components with respect to the magnetic-field direction. The expressions for $K_T^{(\parallel)}$ and $K_T^{(\perp)}$ are given by

$$K_T^{(\parallel)} = \frac{1}{n_B^2} \left(\frac{\partial n_B}{\partial \mu_B} \right)_T, \tag{36}$$

$$K_T^{(\perp)} = \frac{1}{n_B \{ n_B - B(\frac{\partial \mathcal{M}}{\partial \mu_B})_T \}} \left(\frac{\partial n_B}{\partial \mu_B} \right)_T. \tag{37}$$

IV. NUMERICAL RESULTS

In this section we perform a numerical analysis of thermodynamic variables in magnetized nuclear matter. It is well known that the energy-momentum tensor shows anisotropies due to the breaking of spatial rotational symmetry when a finite value of magnetic field is present. Hence, the pressure becomes dependent on the direction of the background magnetic field [48,49]. Since we are interested in the thermodynamic properties of magnetized nuclear matter, we choose two representative values, $eB = 0.02$ GeV^2 and $eB = 0.05$ GeV^2 along with $eB = 0$ which will provide us the opportunity to explore the interplay between the magnetic field and the thermal effects. In this section all the numerical calculations with finite values of background magnetic field will be evaluated by considering up to 1000 Landau levels ensuring the convergence of the results.

A. Mass of nucleon

We begin this section with an investigation of the effective mass of nucleons which is a function of chemical potential, temperature, and magnetic-field strength. Hence, it is necessary to find self-consistent solutions for Eqs. (14) and (15). In Figs. 1(a)–1(c), we show the variation of nucleon mass with chemical potential for several values of temperatures $T = 0$, 10, 20, 30 MeV at different magnetic-field strengths

$eB = 0$, 0.02, 0.05 GeV^2 in the vicinity of liquid-gas phase transition. At $T = 0$, if the effective chemical potential $\mu^\star$ is smaller than the effective energy of the nucleon, then both the scalar density n_s and baryon density n_B will be zero. This can be seen from Eqs. (16) and (17). Hence, at $T = 0$, there is no contribution in effective nucleon mass from the medium. Now, since according to Eq. (15), $\mu_B = \mu^\star$ at $T = 0$ the same holds for μ_B. Therefore, the solution for M remains independent of μ_B leading to a horizontal line in the Figs. 1(a)–1(c) (see magenta line). The medium terms contribute when effective chemical potential $\mu^\star$ is larger than the effective energy of the nucleon. In a certain range of μ_B three solutions are present and hence three distinct values for the nucleon mass exist. In this regime, a first-order phase transition presumably occurs. As the temperature rises, the medium-term contributions tend to reduce the effective nucleon mass as depicted in the figures. Additionally, the existence of multiple solutions for the nucleon mass disappears at a particular value of T and μ_B called critical endpoint (CEP) beyond which the phase transition goes towards the crossover regime. This result is consistent with the previous findings in Ref. [46]. It is also interesting to observe the nucleon mass as a function magnetic field for various values of chemical potential ($\mu_B = 0.3$, 0.7, 1.5 GeV) and temperature ($T = 10$, 20, 30 MeV), as shown in Figs. 2(a) and 2(c). It is evident from the Figs. 2(a) and 2(b) that, for a constant value of μ_B and T, the effective nucleon mass consistently rises with the magnetic field. This phenomenon at low values of μ_B is referred to as magnetic catalysis [46]. However, if the value of μ_B increases [e.g., $\mu_B = 1.5$ GeV in Fig. 2(c)], the variation of effective nucleon mass with eB is marginal.

B. Nuclear liquid-gas phase transition

Now, in Figs. 3(a)–3(c), we illustrate the nuclear liquid-gas phase structure and isentropic curves for various s/n_B values (ranging from 0.05 to 15.0), in the T-μ_B plane under background magnetic fields $eB = 0$, 0.02, 0.05 GeV^2. The isentropic curves depicted in Figs. 3(a) and 3(b) illustrate the trajectories of an ideal fluid under adiabatic conditions. Notably, Fig. 3(b) is a similar plot as Fig. 3(a) in a smaller T-μ_B space. The graphs in Fig. 3(b) exhibit a discernible shift as the magnetic-field strength varies for a specific value of s/n_B. However, as s/n_B increases, the distinctions between the graphs corresponding to the different magnetic-field strengths
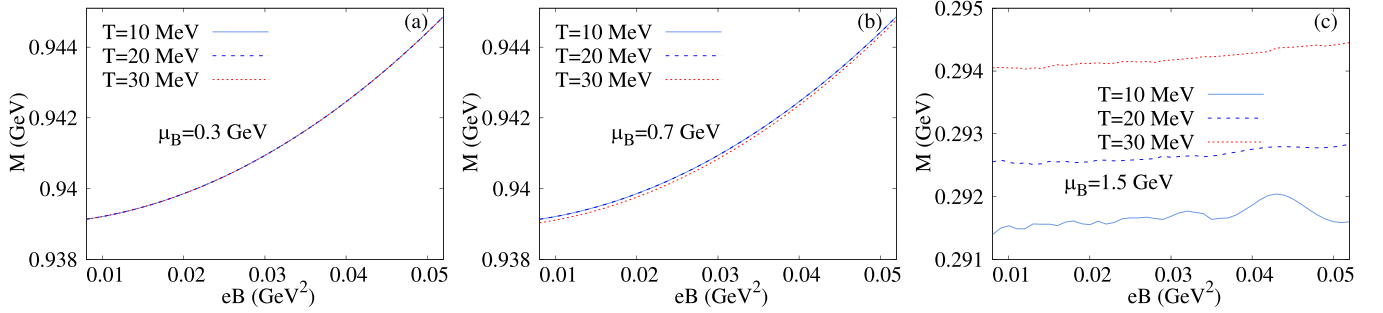
FIG. 2. The effective nucleon mass (M) as a function of background magnetic field eB for different values of temperature $T = 10$, 20, 30 GeV at (a) $\mu_B = 0.3$ GeV, (b) $\mu_B = 0.7$ GeV, (c) $\mu_B = 1.5$ GeV.

decrease. Furthermore, it is evident from Fig. 3(b) that, at $T = 0$, for a given value of eB, the plots for different values of s/n_B meet at a single point on the μ_B axis. This point shifts towards higher μ_B with the increase of magnetic-field strength. This is a reflection of the so-called "magnetic catalysis" observed in Figs. 2(a) and 2(b). Figure 3(c) illustrates the CEP of a liquid-gas phase transition along with the corresponding spinodal lines in the T-μ_B plane for magnetic-field strengths $eB = 0.0$, 0.02, 0.05 GeV^2. The position of CEP shifts towards higher T and lower μ_B as the magnetic-field strength increases. It is to be noted that the spinodal lines are determined from the extrema of $\partial M/\partial T$. This gives rise to two distinct segments of spinodal lines which converge at the CEP, as illustrated in the Fig. 3(c). Notably, the presence of a magnetic field leads to significant changes in the spinodal lines.

C. Magnetization of the medium

In presence of background magnetic field the system will also be magnetized. The expression for the magnetization is given in the Eq. (19). We scale the magnetization of the system as

$$e\mathcal{M}_{\text{scaled}} = \mathcal{M} + B. \tag{38}$$

In Figs. 4(a)–4(c), the dependence of scaled magnetization on the background magnetic field eB is illustrated for different values of the parameter $\mu_B = 1.2$, 1.5, 1.8 GeV. Each subplot corresponds to distinct temperatures: Fig. 4(a) at $T = 10$ MeV, Fig. 4(b) at $T = 15$ MeV, Fig. 4(c) at $T = 25$ MeV.

In Fig. 4(a), it is observed that the positive scaled magnetization shows an oscillating trend with the magnetic field eB. These oscillations can be attributed to the so-called de Haas–van Alphen oscillations [50] of the magnetization in metals and originates from the quantization of the energy levels associated with the orbital motion of charged particles in a magnetic field. Such oscillatory behavior in the magnetization of strongly interacting matter is also observed in Refs. [48,51–53]. Additionally, as the temperature increases, there is a discernible reduction in the oscillating nature of the scaled magnetization, as depicted in Figs. 4(b) and 4(c). It is important to note that the oscillatory behavior observed in the magnetization for NJL-type nonrenormalizable models might be an artifact of the regularization scheme and could vanish for a specific method of regularization [54]. However, the renormalizability of the Walecka model precludes such modifications. This is because the B-dependent vacuum contributions of the thermodynamic potential do not introduce any renormalization scheme dependence in the gap equations or other thermodynamic quantities.

D. Speed of sound at constant s/n_B

In this section, we investigate the variations of the speed of sound with chemical potential in presence of a background magnetic field in nuclear matter. As discussed in Sec. III, in the presence of a magnetic field, C_{s/n_B}^2 splits into $C_{s/n_B}^{2(\parallel)}$ and $C_{s/n_B}^{2(\perp)}$ along and perpendicular to the magnetic-field direction, respectively. To find the speed of sound, we use Eqs. (25)–(29)
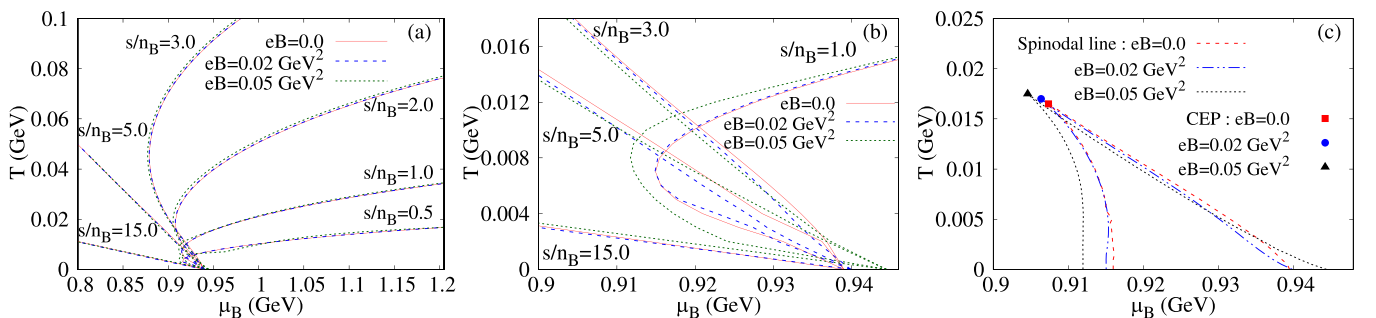
FIG. 3. The isentropic curves for various values of magnetic field eB ($= 0$, 0.02, 0.05 GeV^2) and different values of s/n_B (a) in large T-μ_B plane, (b) in small T-μ_B plane. Different line styles represent specific s/n_B values while a uniform color scheme is used to denote a particular eB value. (c) The spinodal lines and critical endpoints (CEPs) for various values of $eB = 0$, 0.02, 0.05 GeV^2 in T-μ_B plane.
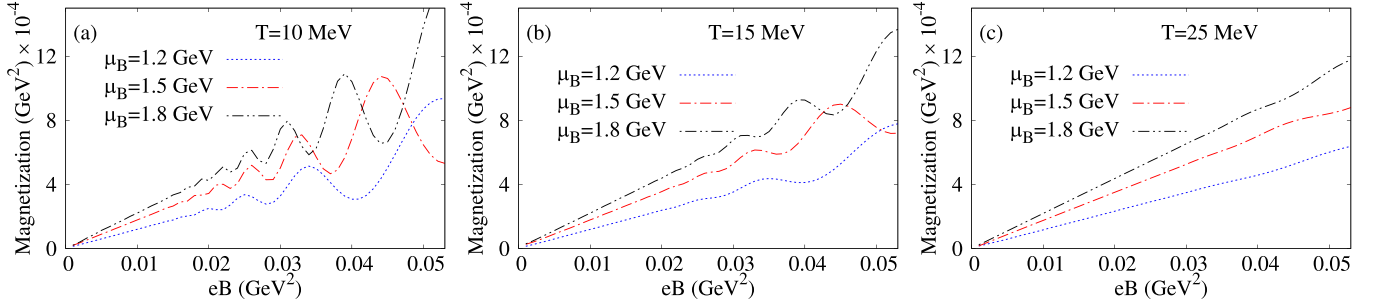
FIG. 4. Scaled magnetization ($\mathcal{M}_{\text{scaled}}$) as a function of eB for $\mu_B = 1.2$, 1.5, 1.8 GeV at (a) $T = 5$ MeV, (b) $T = 10$ MeV, (c) $T = 25$ MeV.

and Eqs. (30)–(34). We plot the parallel component of the squared speed of sound, denoted as $C_{s/n_B}^{2(\parallel)}$, as a function of baryon chemical potential (μ_B) for various temperatures $T = 5$, 10, 16, 25, 50, 100 MeV. These are shown in Fig. 5(a) for the case of zero magnetic-field strength ($eB = 0$), in Fig. 5(b) for $eB = 0.02$ GeV^2, in Fig. 5(c) for $eB = 0.05$ GeV^2. In absence of background magnetic field, it is evident from Fig. 5(a) that $C_{s/n_B}^{2(\parallel)}$ exhibits a steady increase as a function of μ_B for a particular value of temperature. Moreover it can be seen that for smaller values of μ_B, the magnitude of $C_{s/n_B}^{2(\parallel)}$ increases with temperature as the pressure and energy density are dominated by temperature-driven influence. However at large μ_B, the magnitude of $C_{s/n_B}^{2(\parallel)}$ slightly decreases with increasing T. The transition from the region where pressure and energy density are driven by temperature to the region where density-driven effects prevails is presumably due to the factor $(sT + \mu_B n_B)$ present in the denominator of Eq. (25). Furthermore, the transition does not occur at a fixed value of μ_B. Rather this values shifts towards slightly higher values of μ_B with increasing temperature. This is clear from the magnified view of the μ_B dependence of $C_{s/n_B}^{2(\parallel)}$ around $\mu_B \approx 1.38$ GeV provided the inset plot of Fig. 5(a) where $T = 10, 25, 50, 100$ MeV are considered for the clarity of the presentation. Now if we concentrate on the graph for $T = 10$ MeV in the inset plot, then it is evident that as the temperature increases the crossing occurs at higher values of μ_B. In the case of a nonzero magnetic field, as shown in Figs. 5(b) and 5(c), it is also observed that $C_{s/n_B}^{2(\parallel)}$ is larger at high temperature due to the temperature-driven influence on

pressure and energy density at smaller chemical potentials, as in the zero-field case. However, in the domain of higher values of μ_B, no monotonic behavior is observed as in the zero-field case.

Few comments on the magnitude of speed of sound are in order here. In Walecka model at large densities the total pressure is dominated by the vector meson-exchange contribution and in the limit $n_B \to \infty$ it approaches the energy density. Consequently, the speed of sound tends towards the speed of light at large densities [55]. Since the interaction involving the ω meson is proportional to the baryon density, there is a consistent rise in the speed of sound with increasing baryon chemical potential (μ_B), reaching a limiting value of 1 as n_B (or μ_B) approaches infinity. In contrast, NJL-like models present a significantly different scenario. In these models, the value of the sigma mean field and consequently the corresponding interaction, diminishes with increasing density. Thus the NJL-like model behaves like a gas of noninteracting relativistic particles at $n_B \to \infty$. So the Walecka model can be thought to describe nuclear matter and the NJL-like model can give one some insight of high-density quark matter. If a phase transition from nuclear matter to quark matter takes place with growing density, the value of speed of sound is expected to exhibit a peak at a certain density. Recent limits on the speed of sound derived from astrophysical observation were obtained in Ref. [2] using a parametrized EoS and in Ref. [3] in the framework of the chiral effective-field theory and it has been argued that the speed of sound in neutron-star matter may exceed the conformal limit. The speed of sound in neutron-star matter considering different phase-transition
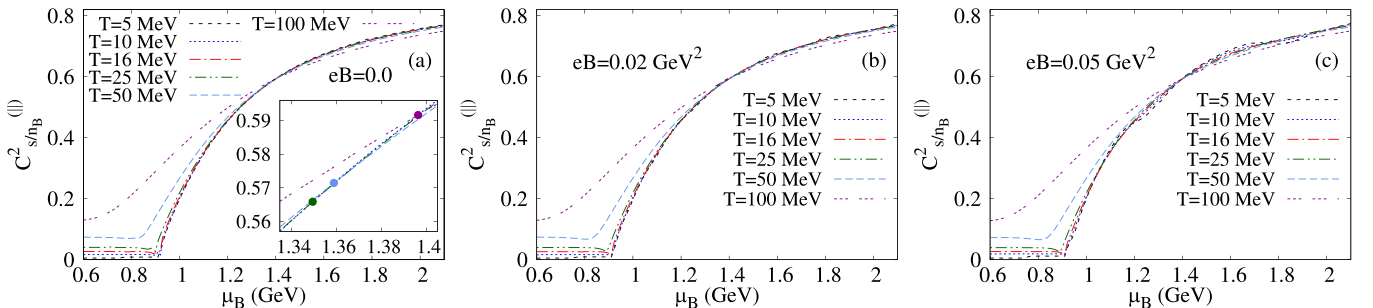
FIG. 5. Parallel component of squared speed of sound $C_{s/n_B}^{2(\parallel)}$ as a function of chemical potential μ_B for a few fixed temperature ($T = 5, 10, 16, 25, 50, 100$ MeV) at (a) $eB = 0$, (b) $eB = 0.02$ GeV^2, (c) $eB = 0.05$ GeV^2.
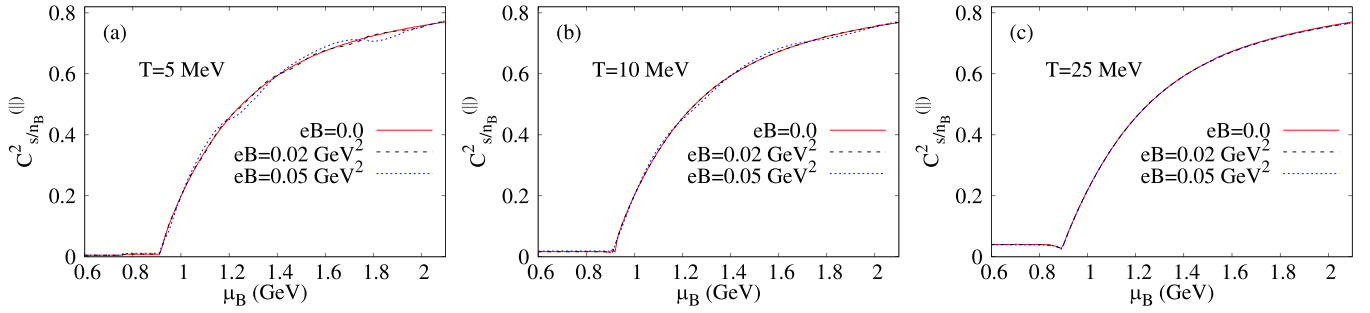
FIG. 6. Parallel component of squared speed of sound $C_{s/n_B}^{2(\parallel)}$ as a function of chemical potential μ_B for $eB = 0.02$, 0.05 GeV^2 at (a) $T = 5$ MeV, (b) $T = 10$ MeV, (c) $T = 25$ MeV.

mechanisms and observational constraints is a topic of ongoing studies [56–58].

The parallel squared speed of sound $C_{s/n_B}^{2(\parallel)}$ is presented as a function of μ_B for different magnetic-field strengths $eB = 0, 0.02, 0.05$ GeV^2 in Fig. 6(a) for $T = 5$ MeV, in Fig. 6(b) for $T = 10$ MeV, and in Fig. 6(c) for $T = 16$ MeV, respectively. In Fig. 6(a), the plots corresponding to nonzero magnetic fields mildly oscillates around the $eB = 0$ plot and the oscillations increase with the increase of magnetic-field strength. As the temperature increases, in Figs. 6(b) and 6(c), the oscillation decreases, i.e., the magnetic field effect decreases. This is also understandable from Figs. 5(b) and 5(c). Therefore, the influence of magnetic field on $C_{s/n_B}^{2(\parallel)}$, which is particularly evident at lower temperatures, demonstrates a diminishing trend as temperature rises.

The variation of $C_{s/n_B}^{2(\perp)}$ with respect to μ_B is plotted for various temperatures $T = 5, 10, 16, 25, 50, 100$ MeV in Fig. 7(a) at $eB = 0.02$ GeV^2 and in Fig. 7(b) at $eB = 0.05$ GeV^2, respectively. Figure 7(a) shows that the oscillating behavior of $C_{s/n_B}^{2(\perp)}$ diminishes with increasing temperature for larger μ_B values. However, in the lower-μ_B domain, $C_{s/n_B}^{2(\perp)}$ rises with temperature. Figure 7(b) shows a similar trend as in Fig. 7(a). The comparison between the parallel and perpendicular components of C_{s/n_B}^2 with respect to μ_B for a temperature of $T = 5$ MeV and a magnetic field of $eB = 0.02$ GeV^2 is illustrated in Fig. 7(c). The figure shows a significant difference between the parallel and perpendicular components of the speed of

sound. In the higher range of μ_B values, the magnitude of $C_{s/n_B}^{2(\parallel)}$ is greater than that of $C_{s/n_B}^{2(\perp)}$.

Figure 8(a) represents $C_{s/n_B}^{2(\perp)}$ as a function of μ_B for background fields $eB = 0.02, 0.05$ GeV at $T = 5$ MeV, while Fig. 8(b) and Fig. 8(c) do so for $T = 10$ MeV and $T = 25$ MeV, respectively. In Figs. 7(a) and 7(b) and 8(a)–8(c), the minima of $C_{s/n_B}^{2(\perp)}$ around $\mu_B = 0.92$ GeV mark the occurrence of the liquid-gas phase transition, which is consistent with $C_{s/n_B}^{2(\perp)}$. Examination of Fig. 8(a) at temperature $T = 5$ MeV reveals that the oscillations in $C_{s/n_B}^{2(\perp)}$ intensify with an increase in the background magnetic field for larger μ_B values. As the temperature rises, the oscillations in $C_{s/n_B}^{2(\perp)}$ diminish [see Fig. 8(b)], achieving a smoother profile [see Fig. 8(c)] for $eB = 0.02, 0.05$ GeV in the domain of higher μ_B values. Conversely, in the domain of lower μ_B values, the values of $C_{s/n_B}^{2(\perp)}$ exhibit an increase with rising temperature. This trend is consistent with the patterns illustrated in Figs. 7(a) and 7(b).

The contour plots in Figs. 9(a)–9(c) demonstrate the profiles of $C_{s/n_B}^{2(\parallel)}$ in the full T-μ_B plane for $eB = 0, 0.02$, and 0.05 GeV^2, respectively. In each of the contour plots the profiles corresponding to $C_{s/n_B}^{2(\parallel)} = 0.1, 0.30, 0.50, 0.75$ are identified separately. Recall that in Figs. 5, 6, and 9 the squared speed of sound is larger than its conformal value, i.e., $1/3$ at high chemical potential or high density. Importantly, causality is always preserved, i.e., $C_{s/n_B}^{2(\parallel)} < 1$. Note that the
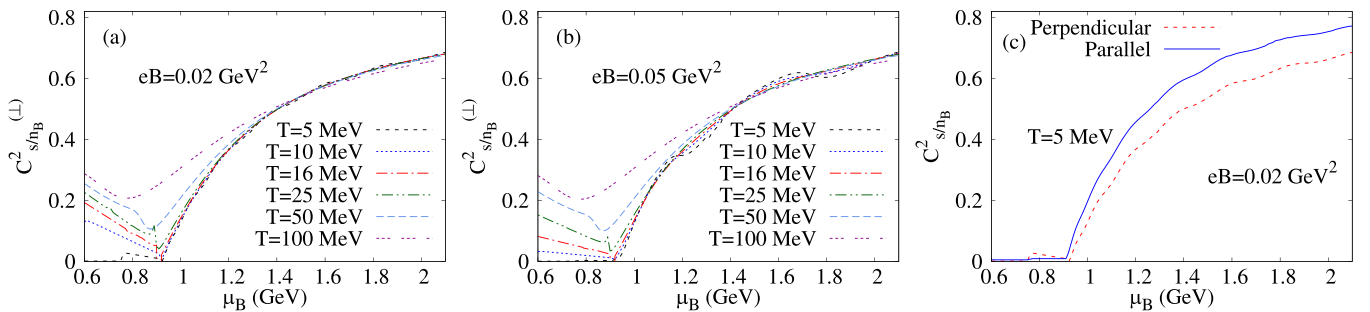
FIG. 7. $C_{s/n_B}^{2(\perp)}$ as a function of chemical potential μ_B for a few fixed temperature ($T = 5, 10, 16, 25, 50, 100$ MeV) at (a) $eB = 0.02$ GeV^2, (b) $eB = 0.05$ GeV^2. Parallel and perpendicular components of C_{s/n_B}^2 as a function of chemical potential μ_B at $T = 5$ MeV and $eB = 0.02$ GeV^2 in panel (a).
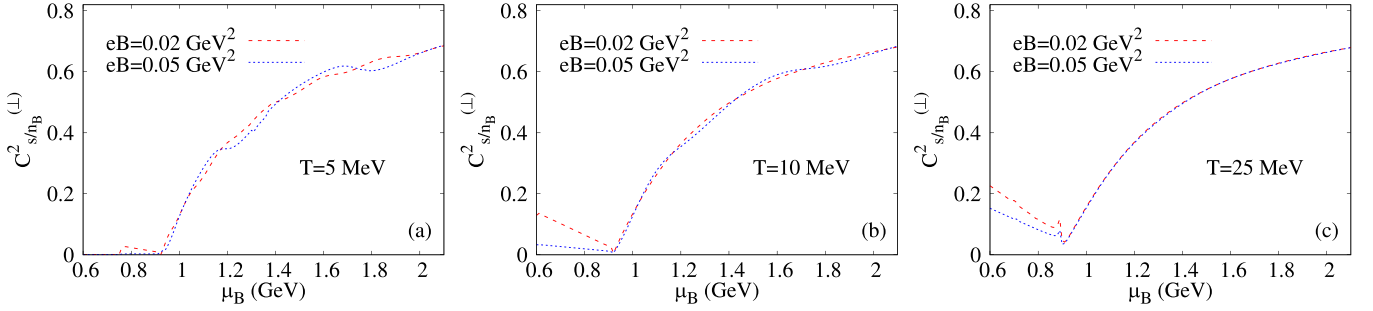
FIG. 8. Perpendicular component of squared speed of sound $C_{s/n_B}^{2(\perp)}$ as a function of chemical potential μ_B for $eB = 0.02,\ 0.05$ GeV^2 at (a) $T = 5$ MeV, (b) $T = 10$ MeV, (c) $T = 25$ MeV.

value of $C_{s/n_B}^{2(\parallel)}$ approaches $1/3$ in quark matter at high chemical potential or high baryon density [17].

E. Speed of sound at constant n_B or s

We present contour maps illustrating $C_{n_B}^{2(\parallel)}$ in the T-μ_B plane under various magnetic-field strengths for $eB = 0$ in Fig. 10(a), $eB = 0.02$ GeV^2 in Fig. 10(b), $eB = 0.05$ GeV^2 in Fig. 10(c). In the absence of a magnetic field, in Fig. 10(a), $C_{n_B}^{2(\parallel)}$ exhibits a nonmonotonic behavior with chemical potential for almost all temperatures. Notably, there is a distinctive peak-like structure observed at intermediate chemical-potential values. When the magnetic field is switched on, these characteristics manifest in a similar fashion. However, at lower temperatures $C_{n_B}^{2(\parallel)}$ exhibits a distinct variation which increases with the increasing magnetic-field strength.

Next, we now show the contour maps of $C_s^{2(\parallel)}$ at constant entropy density under different magnetic-field strengths, specifically, for $eB = 0$ in Fig. 11(a), $eB = 0.02$ GeV^2 in Fig. 11(b), $eB = 0.05$ GeV^2 in Fig. 11(c) respectively. In the absence of magnetic field, as shown in Fig. 11(a), the contour plots of $C_s^{2(\parallel)}$ exhibit a complicated structure. The graphs demonstrate that $C_s^{2(\parallel)}$ has both negative and positive values separated by the red dashed line in the Fig. 11(a). The value of $C_s^{2(\parallel)}$ vanishes on the boundary given by the red dashed line. This feature possibly represents a general phenomenon observed in first-order phase transitions within interacting systems where the fermion mass exhibits a dependency on both temperature and density. A similar behavior in the speed of sound within quark matter is observed in Ref. [17]. Indeed,

the boundary denoted by the red dashed line in Figs. 11(a) can be correlated with the thermodynamic formula

$$\left(\frac{\partial \mu_B}{\partial T}\right)_{s/n_B} = \frac{\mu_B\left(\frac{\partial p^{(\parallel)}}{\partial \epsilon}\right)_s}{T\left(\frac{\partial p^{(\parallel)}}{\partial \epsilon}\right)_{n_B}} = (\mu_B/T)\frac{C_s^{2(\parallel)}}{C_{n_B}^{2(\parallel)}}. \tag{39}$$

Therefore, one can obtain the boundary of $C_s^{2(\parallel)} = 0$ using Eq. (39) and by taking the condition $(\partial \mu_B/\partial T)_{s/n_B} = 0$. Moreover, one of the two physical quantities $C_s^{2(\parallel)}$ and $C_{n_B}^{2(\parallel)}$ takes negative value when $(\partial \mu_B/\partial T)_{s/n_B} < 0$. Since $C_{n_B}^{2(\parallel)}$ is always positive, $C_s^{2(\parallel)}$ is negative in this situation. The region enclosed by the dashed red line in Figs. 11(a) represents this region. With the introduction of a magnetic field, the contour plots exhibit a similar behavior except at lower temperature and high chemical potential, as demonstrated in Figs. 11(b) and 11(c).

F. Speed of sound at constant T

In the following, we explore the speed of sound at constant temperature T. The estimation of $C_T^{2(\parallel)}$ as a function of the baryon number density during the chemical freeze-out of quark-gluon plasma created in relativistic heavy-ion collisions has been carried out in Ref. [59]. In recent times, there has been a lot of discussion regarding the density-dependent $C_T^{2(\parallel)}$ in the context of neutron-star matter. The observational data indicate a substantial value of $C_T^{2(\parallel)}$ (greater than $1/3$) at densities several times that of nuclear saturation. Here, we see the behavior of $C_T^{2(\parallel)}$ in nuclear matter in the full T-μ_B plane under different magnetic-field strengths, specifically, for $eB = 0$ in Fig. 12(a), $eB = 0.02$ GeV^2 in Fig. 12(b),
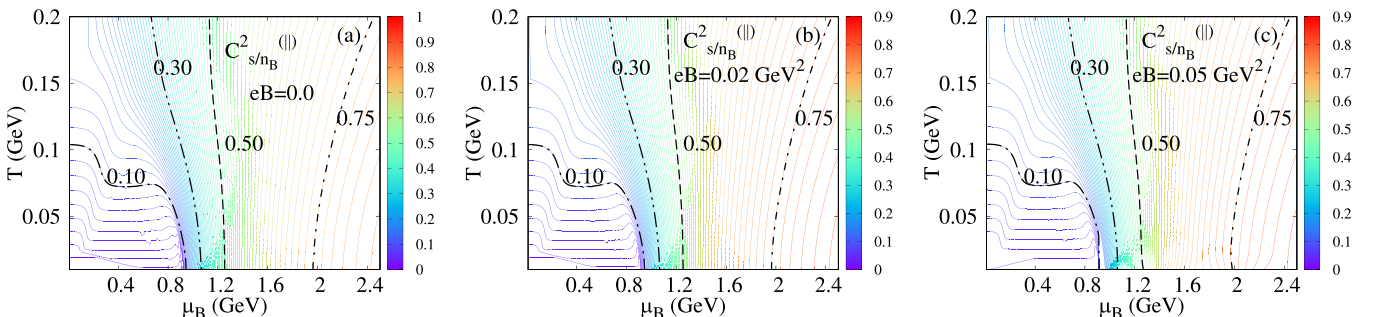
FIG. 9. Contour plots of $C_{s/n_B}^{2(\parallel)}$ in the full T-μ_B plane at (a) $eB = 0$, (b) $eB = 0.02$ GeV^2, (c) $eB = 0.05$ GeV^2.
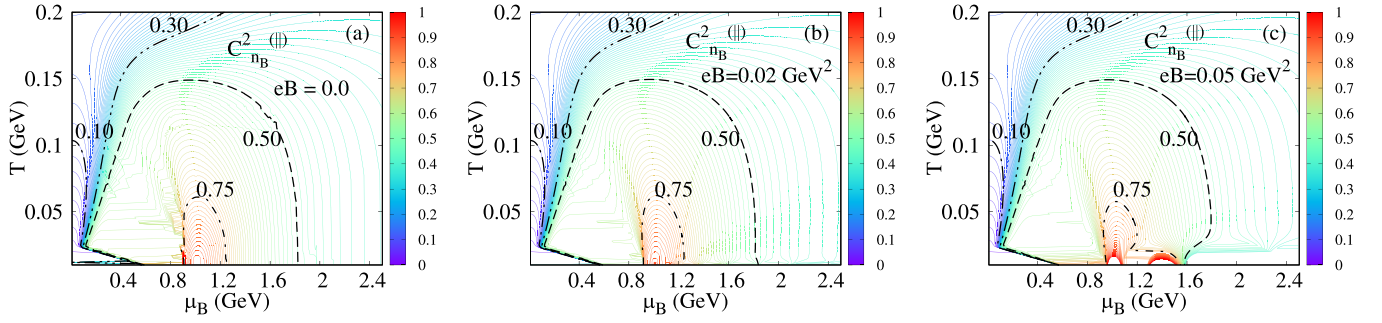
FIG. 10. Contour plots of $C_{n_B}^{2(\parallel)}$ in the full T-μ_B plane at (a) $eB = 0$, (b) $eB = 0.02$ GeV^2, (c) $eB = 0.05$ GeV^2.
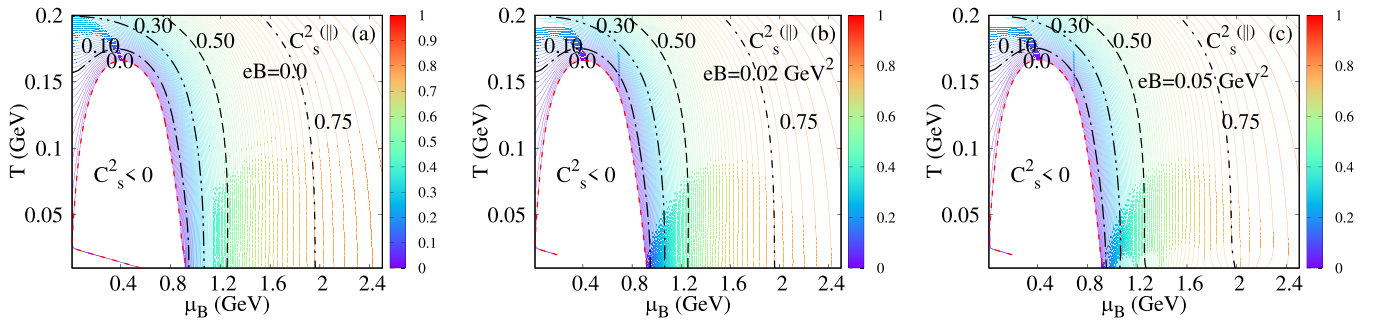
FIG. 11. Contour plots of $C_s^{2(\parallel)}$ in the full T-μ_B plane at (a) $eB = 0$, (b) $eB = 0.02$ GeV^2, (c) $eB = 0.05$ GeV^2.
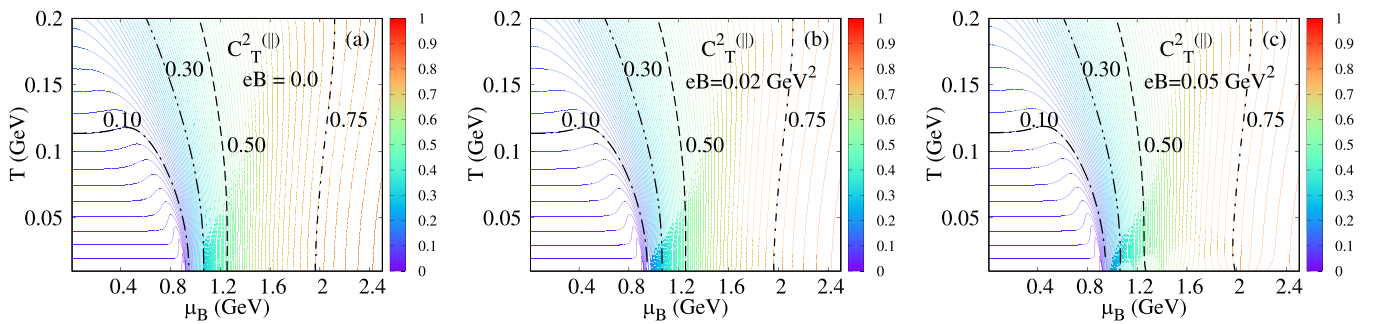
FIG. 12. Contour plots of $C_T^{2(\parallel)}$ in the full T-μ_B plane at (a) $eB = 0$, (b) $eB = 0.02$ GeV^2, (c) $eB = 0.05$ GeV^2.
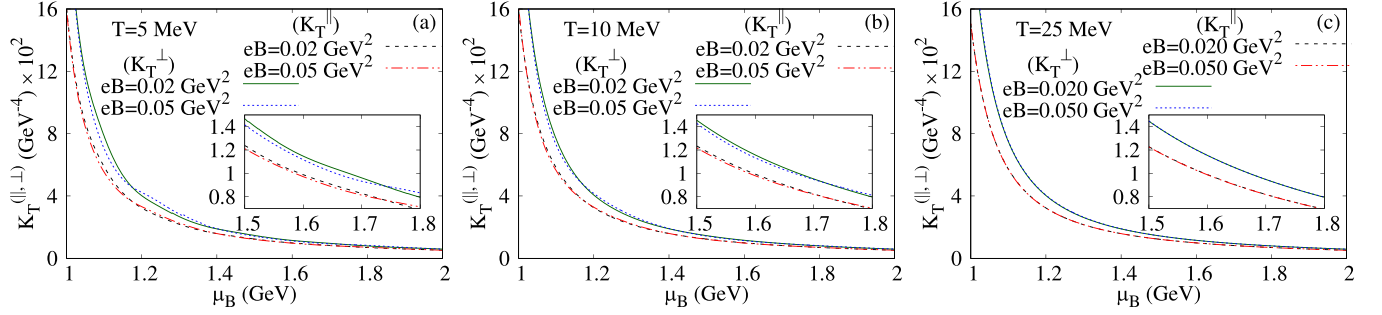
FIG. 13. Parallel and perpendicular components of isothermal compressibility $K_T^{(\parallel, \perp)}$ as a function of μ_B for $eB = 0.02, \ 0.05 \ \text{GeV}^2$ at (a) $T = 5 \ \text{MeV}$, (b) $T = 10 \ \text{MeV}$, (c) $T = 25 \ \text{MeV}$.

$eB = 0.05 \ \text{GeV}^2$ in Fig. 12(c). In the case of zero magnetic field strength in Fig. 12(a), the value of $C_T^{2(\parallel)}$ always increases with the rising chemical potential. At low temperature the behavior of $C_T^{2(\parallel)}$ closely resembles $C_{s/n_B}^{2(\parallel)}$. The effects of the magnetic field are shown in Figs. 12(b) and 12(c).

G. Isothermal compressibility

In the absence of magnetic fields, the isothermal compressibility K_T exhibits isotropy. However, in the presence of magnetic field K_T becomes anisotropic and splits into $K_T^{(\parallel)}$ (along the magnetic-field direction) and $K_T^{(\perp)}$ (perpendicular to the magnetic-field direction). To estimate isothermal compressibility, we use Eqs. (36) and (37). $K_T^{(\parallel, \perp)}$ are plotted as a function of chemical potential μ_B for magnetic field $eB = 0.02, \ 0.05 \ \text{GeV}^2$. The plots are depicted in Fig. 13(a) at $T = 5 \ \text{MeV}$, Fig. 13(b) at $T = 10 \ \text{MeV}$ and Fig. 13(c) at $T = 25 \ \text{MeV}$. Figure 13(a) shows that $K_T^{(\parallel)}$ is smaller than $K_T^{(\perp)}$ for given values of T, μ_B, eB. Therefore, the equation of state is stiffer along the magnetic-field direction. Figures 13(b) and 13(c) show a similar behavior at higher temperatures. In all the graphs both the compressibilities become smaller at higher μ_B indicating a stiffer EoS in this region.

V. SUMMARY AND CONCLUSION

In summary, we have investigated the modifications of nucleon mass, the nuclear liquid-gas phase transition, squared speed of sound and isothermal compressibility in nuclear matter subjected to a background magnetic field at finite temperature and chemical potential (baryon density) within the framework of the nonlinear Walecka model. Our findings reveal that the effective mass of the nucleon increases with the growing background magnetic field, a phenomenon known as magnetic catalysis. Additionally, the presence of a magnetic field is found to influence the positions of the critical endpoint (CEP) and spinodal lines in the T-μ_B plane. Furthermore, our study demonstrates that the presence of magnetic field induces anisotropy in the speed of sound, showing variations between $C_x^{2(\parallel, \perp)}$ components. Our calculations support the assertion that the speed of sound in nuclear matter can exceed $\sqrt{1/3}$ at high chemical potential even in the presence of the magnetic field. However, it is important to note that causality is always upheld, ensuring $C_x^2 < 1$. Notably, we also observed that the influence of the magnetic field on the speed of sound is most pronounced at high chemical potential and low temperature. Moreover, our investigation revealed that the magnetic field can induce anisotropy in the isothermal compressibility of nuclear matter in a similar manner. It is found that $K_T^{(\parallel)}$ is smaller than $K_T^{(\perp)}$ for given values of T, μ_B, eB indicating that the equation of state is stiffer along the magnetic-field direction. It should be noted that the values of temperature and chemical potential considered in this work are more applicable to the case of neutron-star matter. However, the values of the background magnetic field used during the discussions of the numerical results are somewhat higher than expected values in such scenarios. In spite of this the thermodynamic quantities studied in this work exhibit only moderate modifications in the presence of a background magnetic field.

APPENDIX A: eB-DEPENDENT VACUUM CONTRIBUTION

The vacuum contribution to the free energy is

$$\Omega_{\text{sea}} = -2 \int \frac{d^3 k}{(2\pi)^3} E - \frac{qB}{2\pi} \sum_{n=0}^{\infty} \alpha_n \int \frac{dk_z}{2\pi} E_n \tag{A1}$$

$$= -I_0 - I_1 = -2I_0 - (I_1 - I_0), \tag{A2}$$

where

$$I_1 = \frac{qB}{2\pi} \sum_{n=0}^{\infty} \alpha_n \int \frac{dk_z}{2\pi} E_n, \tag{A3}$$

$$I_0 = 2 \int \frac{d^3 k}{(2\pi)^3} E. \tag{A4}$$

The momentum integration in d dimensions is

$$\int \frac{d^n p}{(2\pi)^n} (p^2 + M^2)^{-A} = \frac{\Gamma(A - d/2)}{(4\pi)^{d/2} \Gamma(A)} \left(\frac{1}{M^2}\right)^{A-d/2}. \tag{A5}$$

We first convert the integration in Eq. (A3) into d dimensions and then use the standard dimensional regularization formula (A5) with $A = -1/2$ and $d = 1 - \epsilon \, (\ll 1)$. Thus,

$$I_1 = \frac{(eB)}{2\pi} \frac{\Gamma(-1 + \epsilon/2)}{(4\pi)^{(1-\epsilon)/2} \Gamma(-1/2)} \left[2 \sum_{n=0}^{\infty} \left(\frac{1}{M^2 + 2neB}\right)^{-1+\frac{\epsilon}{2}} - \left(\frac{1}{M^2}\right)^{-1+\frac{\epsilon}{2}} \right]. \tag{A6}$$

Now defining $x = M^2/2eB$ and using the formula of Hurwitz zeta function $\zeta(z, x) = \sum_{n=0}^{\infty} 1/(n + x)^z$, Eq. (A6) can be written as

$$I_1 = -\frac{(eB)^2}{2\pi^2} \left(\frac{eB}{2\pi}\right)^{-\frac{\epsilon}{2}} \Gamma\left(-1 + \frac{\epsilon}{2}\right) \left[\zeta\left(-1 + \frac{\epsilon}{2}, x\right) - \frac{1}{2x^{-1+\frac{\epsilon}{2}}} \right]. \tag{A7}$$

Equation (A7) can be further simplified to obtain

$$I_1 = \frac{(eB)^2}{2\pi^2} \left[-\frac{x^2}{\epsilon} - \frac{1}{2}x^2 + \frac{1}{2}\gamma x^2 + \frac{1}{2}x^2 \ln\frac{eB}{2\pi} + \frac{1}{2}x \ln x + \zeta'(-1, x) \right] + x\text{-independent terms}. \tag{A8}$$

Similarly, we convert the integration in Eq. (A4) into d dimensions using the standard dimensional regularization formula (A5) with $A = -1/2$ and $d = 3 - \epsilon \, (\ll 1)$. Then the simplified equation can be written as

$$I_0 = -\frac{1}{8\pi} M^4 \left(\frac{1}{\epsilon} + \frac{3 - 2\gamma}{4} - \frac{1}{2}\ln M^2 + \frac{1}{2}\ln 4\pi\right). \tag{A9}$$

Inserting $M^2 = 2eBx$ and simplifying, Eq. (A9) can be expressed as

$$I_0 = -\frac{(eB)^2}{2\pi^2} \left[\frac{x^2}{\epsilon} + \frac{3 - 2\gamma}{4}x^2 - \frac{1}{2}x^2 \ln x - \frac{1}{2}x^2 \ln\frac{eB}{2\pi} \right]. \tag{A10}$$

Now

$$\Omega_{\text{sea}} = -2I_0 - (I_1 - I_0) \tag{A11}$$

$$= (2I_0 + x\text{-independent terms}) + \Omega_{\text{vac}}^B, \tag{A12}$$

where eB-dependent vacuum part is

$$\Omega_{\text{vac}}^B = -\frac{(eB)^2}{2\pi^2} \left\{ \zeta'(-1, x) + \frac{1}{4}x^2 + \frac{1}{2}x(1 - x)\ln x \right\}. \tag{A13}$$

APPENDIX B: IMPORTANT THERMODYNAMICS RELATION

$$\left(\frac{\partial \epsilon}{\partial T}\right)_{\mu_B} = T\left(\frac{\partial s}{\partial T}\right)_{\mu_B} + \mu_B\left(\frac{\partial n_B}{\partial T}\right)_{\mu_B}, \quad \left(\frac{\partial \epsilon}{\partial \mu_B}\right)_T = T\left(\frac{\partial s}{\partial \mu_B}\right)_T + \mu_B\left(\frac{\partial n_B}{\partial \mu_B}\right)_T, \tag{B1}$$

$$\left(\frac{\partial(s/n_B)}{\partial \mu_B}\right)_T = \frac{1}{n_B}\left(\frac{\partial s}{\partial \mu_B}\right)_T - \frac{s}{n_B^2}\left(\frac{\partial n_B}{\partial \mu_B}\right)_T, \quad \left(\frac{\partial(s/n_B)}{\partial T}\right)_{\mu_B} = \frac{1}{n_B}\left(\frac{\partial s}{\partial T}\right)_T - \frac{s}{n_B^2}\left(\frac{\partial n_B}{\partial T}\right)_{\mu_B}. \tag{B2}$$

APPENDIX C: SUSCEPTIBILITIES

In Sec. III, we have seen that the speed of sound contain $(\partial\mathcal{M}/\partial T)_{\mu_B}$, $(\partial\mathcal{M}/\partial\mu_B)_T$, $(\partial s/\partial\mu_B)_T$, $(\partial s/\partial T)_{\mu_B}$, $(\partial n_B/\partial\mu_B)_T$, $(\partial n_B/\partial T)_{\mu_B}$ and can be obtained from the free energy Ω. The expressions are given below:

$$
\left(\frac{\partial\mathcal{M}}{\partial T}\right)_{\mu_B} = -\frac{M}{2\pi^2}\left[2x(1-\ln x)+\ln\Gamma(x)+x(\Psi(x)-1)+\frac{1}{2}\left(1+\ln\frac{x}{2\pi}\right)\right]\frac{\partial M}{\partial T} - \sum_{n=0}^{\infty}\alpha_n\int\frac{dp_z}{4\pi^2}[\ln(1-f_n^+)+\ln(1-f_n^-)]
$$

$$
-T\sum_{n=0}^{\infty}\alpha_n\int\frac{dp_z}{4\pi^2}\left[-\frac{E_n}{T^2}(f_n^++f_n^-)-\frac{\mu^\star}{T^2}(f_n^--f_n^+)+\frac{1}{T}\frac{M}{E_n}\frac{\partial M}{\partial T}(f_n^++f_n^-)+\frac{1}{T}\frac{\partial\mu^\star}{\partial T}(f_n^--f_n^+)\right]
$$

$$
-eB\sum_{n=0}^{\infty}\alpha_n\int\frac{dp_z}{4\pi^2}\frac{n}{E_n}\left[-\frac{M}{E_n^2}\frac{\partial M}{\partial T}(f_n^++f_n^-)+\frac{1}{T^2}\{(E_n+\mu^\star)f^-(1-f^-)+(E_n-\mu^\star)f_n^+(1-f_n^+)\}\right.
$$

$$
\left.-\frac{1}{T}\frac{M}{E_n}\frac{\partial M}{\partial T}\{f_n^+(1-f_n^+)+f_n^-(1-f_n^-)\}-\frac{1}{T}\frac{\partial\mu^\star}{\partial T}\{f_n^-(1-f_n^-)-f_n^+(1-f_n^+)\}\right], \tag{C1}
$$

$$
\left(\frac{\partial\mathcal{M}}{\partial\mu_B}\right)_T = -\frac{M}{2\pi^2}\left[2x(1-\ln x)+\ln\Gamma(x)+x(\Psi(x)-1)+\frac{1}{2}\left(1+\ln\frac{x}{2\pi}\right)\right]\frac{\partial M}{\partial\mu_B}
$$

$$
-\sum_{n=0}^{\infty}\alpha_n\int\frac{dp_z}{4\pi^2}\left[\frac{M}{E_n}\frac{\partial M}{\partial\mu_B}(f_n^++f_n^-)+\frac{\partial\mu^\star}{\partial\mu_B}(f_n^--f_n^+)\right]+qB\sum_{n=0}^{\infty}\alpha_n\int\frac{dp_z}{4\pi^2}\frac{n}{E_n^3}M(f_n^++f_n^-)\frac{\partial M}{\partial\mu_B}
$$

$$
-\frac{eB}{T}\sum_{n=0}^{\infty}\alpha_n\int\frac{dp_z}{4\pi^2}\frac{n}{E_n}\left[\frac{M}{E_n}\frac{\partial M}{\partial\mu_B}\{f_n^+(1-f_n^+)+f_n^-(1-f_n^-)\}+\frac{\partial\mu^\star}{\partial\mu}\{f_n^-(1-f_n^-)-f_n^+(1-f_n^+)\}\right], \tag{C2}
$$

where $\Psi(x)=\frac{\partial}{\partial x}[\ln\Gamma(x)]$ is digamma function and

$$
\left(\frac{\partial s}{\partial T}\right)_{\mu_B} = \int\frac{d^3k}{(2\pi)^3}\frac{1}{T^2}\left[\left\{\frac{E-\mu^\star}{T}-\frac{M}{E}\frac{\partial M}{\partial T}+\frac{\partial\mu^\star}{\partial T}\right\}(E-\mu^\star)f^+(1-f^+)+\left\{\frac{E+\mu^\star}{T}-\frac{M}{E}\frac{\partial M}{\partial T}-\frac{\partial\mu^\star}{\partial T}\right\}\right.
$$

$$
\left.\times(E+\mu^\star)f^-(1-f^-)\right]
$$

$$
+\frac{qB}{2\pi}\sum_{n=0}^{\infty}\alpha_n\int\frac{dk_z}{2\pi}\frac{1}{T^2}\left[\left\{\frac{E_n-\mu^\star}{T}-\frac{M}{E_n}\frac{\partial M}{\partial T}+\frac{\partial\mu^\star}{\partial T}\right\}(E_n-\mu^\star)f_n^+(1-f_n^+)+\left\{\frac{E_n+\mu^\star}{T}-\frac{M}{E_n}\frac{\partial M}{\partial T}-\frac{\partial\mu^\star}{\partial T}\right\}\right.
$$

$$
\left.\times(E_n+\mu^\star)f_n^-(1-f_n^-)\right], \tag{C3}
$$

$$
\left(\frac{\partial s}{\partial\mu_B}\right)_T = -\frac{qB}{2\pi}\frac{1}{T^2}\sum_{n=0}^{\infty}\alpha_n\int\frac{dk_z}{2\pi}\left[\left\{\frac{M}{E_n}\frac{\partial M}{\partial\mu_B}-\frac{\partial\mu^\star}{\partial\mu_B}\right\}(E_n-\mu^\star)f_n^+(1-f_n^+)+\left\{\frac{M}{E_n}\frac{\partial M}{\partial\mu_B}+\frac{\partial\mu^\star}{\partial\mu_B}\right\}(E_n+\mu^\star)f_n^-(1-f_n^-)\right]
$$

$$
-\frac{2}{T^2}\int\frac{d^3k}{(2\pi)^3}\left[\left\{\frac{M}{E}\frac{\partial M}{\partial\mu_B}-\frac{\partial\mu^\star}{\partial\mu_B}\right\}(E-\mu^\star)f^+(1-f^+)+\left\{\frac{M}{E}\frac{\partial M}{\partial\mu_B}+\frac{\partial\mu^\star}{\partial\mu_B}\right\}(E+\mu^\star)f^-(1-f^-)\right], \tag{C4}
$$

$$
\left(\frac{\partial n_B}{\partial T}\right)_{\mu_B} = \frac{qB}{2\pi}\sum_{n=0}^{\infty}\alpha_n\int\frac{dk_z}{2\pi}\left[\left\{\frac{E_n-\mu^\star}{T^2}-\frac{1}{T}\left(\frac{M}{E_n}\frac{\partial M}{\partial T}-\frac{\partial\mu^\star}{\partial T}\right)\right\}f_n^+(1-f_n^+)\right.
$$

$$
\left.-\left\{\frac{E_n+\mu^\star}{T^2}-\frac{1}{T}\left(\frac{M}{E_n}\frac{\partial M}{\partial T}+\frac{\partial\mu^\star}{\partial T}\right)\right\}f_n^-(1-f_n^-)\right]
$$

$$
+2\int\frac{d^3k}{(2\pi)^3}\left[\left\{\frac{E-\mu^\star}{T^2}-\frac{1}{T}\left(\frac{M}{E}\frac{\partial M}{\partial T}-\frac{\partial\mu^\star}{\partial T}\right)\right\}f^+(1-f^+)-\left\{\frac{E+\mu^\star}{T^2}-\frac{1}{T}\left(\frac{M}{E}\frac{\partial M}{\partial T}+\frac{\partial\mu^\star}{\partial T}\right)\right\}f^-(1-f^-)\right]
$$

$$
\tag{C5}
$$

$$
= Y_T + Y_M\frac{\partial M}{\partial T}+Y_{\mu^\star}\frac{\partial\mu^\star}{\partial T}, \tag{C6}
$$

$$\left(\frac{\partial n_B}{\partial \mu_B}\right)_T = \frac{qB}{2\pi}\sum_{n=0}^{\infty}\alpha_n \int \frac{dk_z}{2\pi}\left[-\frac{1}{T}\left(\frac{M}{E_n}\frac{\partial M}{\partial \mu_B} - \frac{\partial \mu^\star}{\partial \mu_B}\right)f_n^+(1-f_n^+) + \frac{1}{T}\left(\frac{M}{E_n}\frac{\partial M}{\partial \mu_B} + \frac{\partial \mu^\star}{\partial \mu_B}\right)f_n^-(1-f_n^-)\right]$$

$$+ 2\int \frac{d^3k}{(2\pi)^3}\left[-\frac{1}{T}\left(\frac{M}{E}\frac{\partial M}{\partial \mu_B} - \frac{\partial \mu^\star}{\partial \mu_B}\right)f^+(1-f^+) + \frac{1}{T}\left(\frac{M}{E}\frac{\partial M}{\partial \mu_B} + \frac{\partial \mu^\star}{\partial \mu_B}\right)f^-(1-f^-)\right] \tag{C7}$$

$$= Y_M\frac{\partial M}{\partial \mu_B} + Y_{\mu^\star}\frac{\partial \mu^\star}{\partial \mu_B}, \tag{C8}$$

$$\left(\frac{\partial n_s}{\partial T}\right)_{\mu_B} = 2\int \frac{d^3k}{(2\pi)^3}\left(\frac{1}{E} - \frac{M^2}{E^3}\right)\frac{\partial M}{\partial T}(f^+ + f^-) + \frac{eB}{2\pi}\sum_{n=0}^{\infty}\alpha_n \int \frac{dk_z}{2\pi}\left(\frac{1}{E_n} - \frac{M^2}{E_n^3}\right)\frac{\partial M}{\partial T}(f_n^+ + f_n^-)$$

$$+ 2\int \frac{d^3k}{(2\pi)^3}\frac{M}{E}\left[\left\{\frac{E+\mu^\star}{T^2} - \frac{1}{T}\left(\frac{M}{E}\frac{\partial M}{\partial T} + \frac{\partial \mu^\star}{\partial T}\right)\right\}f^-(1-f^-)\right.$$

$$+ \left\{\frac{E-\mu^\star}{T^2} - \frac{1}{T}\left(\frac{M}{E}\frac{\partial M}{\partial T} - \frac{\partial \mu^\star}{\partial T}\right)\right\}f^+(1-f^+)\right]$$

$$+ \frac{eB}{2\pi}\sum_{n=0}^{\infty}\alpha_n \int \frac{dk_z}{2\pi}\frac{M}{E_n}\left[\left\{\frac{E_n+\mu^\star}{T^2} - \frac{1}{T}\left(\frac{M}{E_n}\frac{\partial M}{\partial T} + \frac{\partial \mu^\star}{\partial T}\right)\right\}f_n^-(1-f_n^-)\right.$$

$$+ \left\{\frac{E_n-\mu^\star}{T^2} - \frac{1}{T}\left(\frac{M}{E_n}\frac{\partial M}{\partial T} - \frac{\partial \mu^\star}{\partial T}\right)\right\}f_n^+(1-f_n^+)\right]$$

$$= X_T + X_M\frac{\partial M}{\partial T} + X_{\mu^\star}\frac{\partial \mu^\star}{\partial T}, \tag{C9}$$

$$\left(\frac{\partial n_s}{\partial \mu_B}\right)_T = 2\int \frac{d^3k}{(2\pi)^3}\left(\frac{1}{E} - \frac{M^2}{E^3}\right)\frac{\partial M}{\partial \mu_B}(f^+ + f^-) + \frac{eB}{2\pi}\sum_{n=0}^{\infty}\alpha_n \int \frac{dk_z}{2\pi}\left(\frac{1}{E_n} - \frac{M^2}{E_n^3}\right)\frac{\partial M}{\partial \mu_B}(f_n^+ + f_n^-)$$

$$+ 2\int \frac{d^3k}{(2\pi)^3}\frac{M}{E}\left[\left\{-\frac{1}{T}\left(\frac{M}{E}\frac{\partial M}{\partial \mu_B} + \frac{\partial \mu^\star}{\partial \mu_B}\right)\right\}f^-(1-f^-) + \left\{-\frac{1}{T}\left(\frac{M}{E}\frac{\partial M}{\partial \mu_B} - \frac{\partial \mu^\star}{\partial \mu_B}\right)\right\}f^+(1-f^+)\right]$$

$$+ \frac{eB}{2\pi}\sum_{n=0}^{\infty}\alpha_n \int \frac{dk_z}{2\pi}\frac{M}{E_n}\left[\left\{-\frac{1}{T}\left(\frac{M}{E_n}\frac{\partial M}{\partial \mu_B} + \frac{\partial \mu^\star}{\partial \mu_B}\right)\right\}f_n^-(1-f_n^-) + \left\{-\frac{1}{T}\left(\frac{M}{E_n}\frac{\partial M}{\partial \mu_B} - \frac{\partial \mu^\star}{\partial \mu_B}\right)\right\}f_n^+(1-f_n^+)\right]$$

$$= X_M\frac{\partial M}{\partial \mu_B} + X_{\mu^\star}\frac{\partial \mu^\star}{\partial \mu_B}, \tag{C10}$$

where

$$X_T = 2\int \frac{d^3k}{(2\pi)^3}\frac{M}{E}\frac{1}{T^2}\{(E+\mu^\star)f^-(1-f^-) + (E-\mu^\star)f^+(1-f^+)\}$$

$$+ \frac{eB}{2\pi}\sum_{n=0}^{\infty}\alpha_n \int \frac{dk_z}{2\pi}\frac{M}{E_n}\frac{1}{T^2}\{(E_n+\mu^\star)f_n^-(1-f_n^-) + (E_n-\mu^\star)f_n^+(1-f_n^+)\}, \tag{C11}$$

$$X_M = 2\int \frac{d^3k}{(2\pi)^3}\left[\left(\frac{1}{E} - \frac{M^2}{E^3}\right)(f^+ + f^-) - \frac{1}{T}\left(\frac{M}{E}\right)^2\{f^+(1-f^+) + f^-(1-f^-)\}\right]$$

$$+ \frac{eB}{2\pi}\sum_{n=0}^{\infty}\alpha_n \int \frac{dk_z}{2\pi}\left[\left(\frac{1}{E_n} - \frac{M^2}{E_n^3}\right)(f_n^+ + f_n^-) - \frac{1}{T}\left(\frac{M}{E_n}\right)^2\{f_n^+(1-f_n^+) + f_n^-(1-f_n^-)\}\right], \tag{C12}$$

$$X_{\mu^\star} = 2\int \frac{d^3k}{(2\pi)^3}\frac{1}{T}\frac{M}{E}\{f^+(1-f^+) - f^-(1-f^-)\} + \frac{eB}{2\pi}\sum_{n=0}^{\infty}\alpha_n \int \frac{dk_z}{2\pi}\frac{1}{T}\frac{M}{E_n}\{f_n^+(1-f_n^+) - f_n^-(1-f_n^-)\}, \tag{C13}$$

$$Y_T = 2 \int \frac{d^3k}{(2\pi)^3} \frac{1}{T^2} \{(E - \mu^\star)f^+(1 - f^+) - (E + \mu^\star)f^-(1 - f^-)\}$$

$$+ \frac{eB}{2\pi} \sum_{n=0}^{\infty} \alpha_n \int \frac{dk_z}{2\pi} \frac{1}{T^2} \{(E_n - \mu^\star)f_n^+(1 - f_n^+) - (E_n + \mu^\star)f_n^-(1 - f_n^-)\}, \tag{C14}$$

$$Y_M = 2 \int \frac{d^3k}{(2\pi)^3} \frac{1}{T} \frac{M}{E} \{-f^+(1 - f^+) + f^-(1 - f^-)\} + \frac{eB}{2\pi} \sum_{n=0}^{\infty} \alpha_n \int \frac{dk_z}{2\pi} \frac{1}{T} \frac{M}{E_n} \{-f_n^+(1 - f_n^+) + f_n^-(1 - f_n^-)\}, \tag{C15}$$

$$Y_{\mu^\star} = 2 \int \frac{d^3k}{(2\pi)^3} \frac{1}{T} \{f^+(1 - f^+) + f^-(1 - f^-)\} + \frac{eB}{2\pi} \sum_{n=0}^{\infty} \alpha_n \int \frac{dk_z}{2\pi} \frac{1}{T} \{f_n^+(1 - f_n^+) + f_n^-(1 - f_n^-)\}. \tag{C16}$$

The derivatives $\partial M/\partial T$, $\partial \mu^\star/\partial T$, $\partial M/\partial \mu_B$, and $\partial \mu^\star/\partial \mu_B$ in Eqs. (C3), (C4), (C5), and (C7) can be obtained analytically from Eqs. (14)–(17) and are given by the matrix equations as

$$\begin{pmatrix} f' - X_M & -X_{\mu^\star} \\ Y_M & Y_{\mu^\star} + \frac{1}{(g_\omega/m_\omega)^2} \end{pmatrix} \begin{pmatrix} \frac{\partial M}{\partial T} \\ \frac{\partial \mu^\star}{\partial T} \end{pmatrix} = \begin{pmatrix} X_T \\ -Y_T \end{pmatrix}, \tag{C17}$$

$$\begin{pmatrix} f' - X_M & -X_{\mu^\star} \\ Y_M & Y_{\mu^\star} + \frac{1}{(g_\omega/m_\omega)^2} \end{pmatrix} \begin{pmatrix} \frac{\partial M}{\partial \mu_B} \\ \frac{\partial \mu^\star}{\partial \mu_B} \end{pmatrix} = \begin{pmatrix} 0 \\ \frac{1}{(g_\omega/m_\omega)^2} \end{pmatrix}, \tag{C18}$$

where

$$f = -\frac{M - m_N}{(g_\sigma/m_\sigma)^2} + bm_N(m_N - M)^2 + c(m_N - M)^3 + \frac{qB}{2\pi^2} M \left\{ x(1 - \ln x) + \frac{1}{2} \ln \frac{x}{2\pi} + \ln \Gamma(x) \right\}, \tag{C19}$$

$$f' = \frac{\partial f(M)}{\partial M} = -\frac{1}{(g_\sigma/m_\sigma)^2} - 2bm_N(m_N - M) - 3c(m_N - M)^2$$

$$+ \frac{eB}{2\pi^2} \left\{ x(1 - \ln x) + \frac{1}{2} \ln \frac{x}{2\pi} + \ln \Gamma(x) \right\} + \frac{M^2}{2\pi^2} \left\{ \Psi(x) + \frac{1}{2x} - \ln x \right\}. \tag{C20}$$

[1] F. Özel and P. Freire, Annu. Rev. Astron. Astrophys. **54**, 401 (2016).

[2] P. Bedaque and A. W. Steiner, Phys. Rev. Lett. **114**, 031103 (2015).

[3] I. Tews, J. Carlson, S. Gandolfi, and S. Reddy, Astrophys. J. **860**, 149 (2018).

[4] L. McLerran and S. Reddy, Phys. Rev. Lett. **122**, 122701 (2019).

[5] Y. Fujimoto, K. Fukushima, and K. Murase, Phys. Rev. D **101**, 054016 (2020).

[6] P. Jaikumar, A. Semposki, M. Prakash, and C. Constantinou, Phys. Rev. D **103**, 123009 (2021).

[7] J. Adams *et al.* (STAR Collaboration), Nucl. Phys. A **757**, 102 (2005).

[8] S. Borsanyi, Z. Fodor, J. N. Guenther, R. Kara, S. D. Katz, P. Parotto, A. Pásztor, C. Ratti, and K. K. Szabó, Phys. Rev. Lett. **125**, 052001 (2020).

[9] S. Borsányi, Z. Fodor, S. D. Katz, S. Krieg, C. Ratti, and K. K. Szabó, Phys. Rev. Lett. **111**, 062005 (2013).

[10] Y. Aoki, G. Endrodi, Z. Fodor, S. D. Katz, and K. K. Szabó, Nature (London) **443**, 675 (2006).

[11] A. Bazavov *et al.* (HotQCD Collaboration), Phys. Rev. D **90**, 094503 (2014).

[12] K. Fukushima, Phys. Rev. D **77**, 114028 (2008); **78**, 039902(E) (2008).

[13] S.-X. Qin, L. Chang, H. Chen, Y.-X. Liu, and C. D. Roberts, Phys. Rev. Lett. **106**, 172301 (2011).

[14] W.-J. Fu, J. M. Pawlowski, and F. Rennecke, Phys. Rev. D **101**, 054032 (2020).

[15] A. Bazavov *et al.* (HotQCD Collaboration), Phys. Lett. B **795**, 15 (2019).

[16] O. Philipsen, Prog. Part. Nucl. Phys. **70**, 55 (2013).

[17] W.-b. He, G.-y. Shao, X.-y. Gao, X.-r. Yang, and C.-l. Xie, Phys. Rev. D **105**, 094024 (2022).

[18] R. Marty, E. Bratkovskaya, W. Cassing, J. Aichelin, and H. Berrehrah, Phys. Rev. C **88**, 045204 (2013).

[19] J. Peterson, P. Costa, R. Kumar, V. Dexheimer, R. Negreiros, and C. Providência, Phys. Rev. D **108**, 063011 (2023).

[20] A. Abhishek, H. Mishra, and S. Ghosh, Phys. Rev. D **97**, 014005 (2018).

[21] B.-J. Schaefer, M. Wagner, and J. Wambach, Phys. Rev. D **81**, 074013 (2010).

[22] R. Venugopalan and M. Prakash, Nucl. Phys. A **546**, 718 (1992).

[23] M. Bluhm, P. Alba, W. Alberico, A. Beraudo, and C. Ratti, Nucl. Phys. A **929**, 157 (2014).

[24] Z. V. Khaidukov, M. S. Lukashov, and Y. A. Simonov, Phys. Rev. D **98**, 074031 (2018).

[25] Z. V. Khaidukov and Y. A. Simonov, Phys. Rev. D **100**, 076009 (2019).

[26] V. Mykhaylova and C. Sasaki, Phys. Rev. D **103**, 014007 (2021).

[27] D. E. Kharzeev, L. D. McLerran, and H. J. Warringa, Nucl. Phys. A **803**, 227 (2008).

[28] V. Skokov, A. Y. Illarionov, and V. Toneev, Int. J. Mod. Phys. A **24**, 5925 (2009).

[29] K. Tuchin, Phys. Rev. C **88**, 024911 (2013).

[30] U. Gursoy, D. Kharzeev, and K. Rajagopal, Phys. Rev. C **89**, 054905 (2014).

[31] G. Inghirami, L. Del Zanna, A. Beraudo, M. H. Moghaddam, F. Becattini, and M. Bleicher, Eur. Phys. J. C **76**, 659 (2016).

[32] P. Kalikotay, S. Ghosh, N. Chaudhuri, P. Roy, and S. Sarkar, Phys. Rev. D **102**, 076007 (2020).

[33] Z. Wang, J. Zhao, C. Greiner, Z. Xu, and P. Zhuang, Phys. Rev. C **105**, L041901 (2022).

[34] I. A. Shovkovy, Particles **5**, 442 (2022).

[35] R. C. Duncan and C. Thompson, Astrophys. J. **392**, L9 (1992).

[36] C. Thompson and R. C. Duncan, Astrophys. J. **408**, 194 (1993).

[37] G. Prakash Kadam, Mod. Phys. Lett. A **30**, 1550031 (2015).

[38] A. Das, H. Mishra, and R. K. Mohapatra, Phys. Rev. D **100**, 114004 (2019).

[39] A. Dash, S. Samanta, J. Dey, U. Gangopadhyaya, S. Ghosh, and V. Roy, Phys. Rev. D **102**, 016016 (2020).

[40] R. Ghosh and N. Haque, Phys. Rev. D **105**, 114029 (2022).

[41] A. Das, H. Mishra, and R. K. Mohapatra, Phys. Rev. D **99**, 094031 (2019).

[42] R. Mondal, N. Chaudhuri, S. Ghosh, S. Sarkar, and P. Roy, Phys. Rev. D **107**, 036017 (2023).

[43] R. Mondal, N. Chaudhuri, S. Ghosh, S. Sarkar, and P. Roy, Eur. Phys. J. A **59**, 287 (2023).

[44] A. Mukherjee, S. Ghosh, M. Mandal, S. Sarkar, and P. Roy, Phys. Rev. D **98**, 056024 (2018).

[45] W.-B. He, G.-Y. Shao, and C.-L. Xie, Phys. Rev. C **107**, 014903 (2023).

[46] A. Haber, F. Preis, and A. Schmitt, Phys. Rev. D **90**, 125036 (2014).

[47] J. W. Negele and E. Vogt, *Advances in Nuclear Physics* (Plenum Press, New York, 1986), Vol. 16.

[48] E. J. Ferrer, V. de la Incera, J. P. Keith, I. Portillo, and P. L. Springsteen, Phys. Rev. C **82**, 065802 (2010).

[49] E. J. Ferrer and A. Hackebill, Nucl. Phys. A **1031**, 122608 (2023).

[50] L. D. Landau and E. M. Lifshitz, *Statistical Physics, Part 1*, Course of Theoretical Physics (Butterworth-Heinemann, Oxford, 1980), Vol. 5.

[51] J. L. Noronha and I. A. Shovkovy, Phys. Rev. D **76**, 105030 (2007); **86**, 049901(E) (2012).

[52] X.-G. Huang, M. Huang, D. H. Rischke, and A. Sedrakian, Phys. Rev. D **81**, 045015 (2010).

[53] D. P. Menezes, M. B. Pinto, and C. Providência, Phys. Rev. C **97**, 029904(E) (2018).

[54] S. S. Avancini, R. L. S. Farias, N. N. Scoccola, and W. R. Tavares, Phys. Rev. D **99**, 116002 (2019).

[55] A. Schmitt, *Dense Matter in Compact Stars: A Pedagogical Introduction* (2010), Vol. 811, pp. 1–111.

[56] J. R. Stone, V. Dexheimer, P. A. M. Guichon, A. W. Thomas, and S. Typel, Mon. Not. R. Astron. Soc. **502**, 3476 (2021).

[57] S. Pal, S. Podder, D. Sen, and G. Chaudhuri, Phys. Rev. D **107**, 063019 (2023).

[58] V. Dexheimer, J. Noronha, J. Noronha-Hostler, C. Ratti, and N. Yunes, J. Phys. G **48**, 073001 (2021).

[59] A. Sorensen, D. Oliinychenko, V. Koch, and L. McLerran, Phys. Rev. Lett. **127**, 042303 (2021).